UNIVERSAL WISER
PUBLISHER

Article

Modulation of the laser-induced phase transition of VO$_2$/W-TiO$_2$ *n-n* heterojunction

Weizheng Shi, Leran Zhao, Qiujing Xu, Yushan Zheng, Juncheng Liu*

School of Materials Science and Engineering, Tiangong University, Tianjin, 300387 China

*Corresponding author, Juncheng Liu, jchliu@tiangong.edu.cn

Abstract: To solve the contradiction between the low phase transition threshold and the infrared switching efficiency (*r*) of VO$_2$, the VO$_2$/W-TiO$_2$ *n-n* heterojunction was fabricated on the K9 glass substrate with the magnetron sputtering. The effects of W doping for TiO$_2$ layer on the heterojunction phase transition performance were investigated. An appropriate W doping increases the carrier concentration (*n*) and its mobility (*μ*), thereby reducing both the thermotropic phase transition threshold (*T*$_c$) and the laser-induced phase transition threshold (*P*$_c$) of the heterojunction. The heterojunction doped 1.37 at% W exhibits the optimal comprehensive performance. The *r* of the heterojunction is up to 56.8%, the Tc decreases to 54.3 °C, and the *P*$_c$ to 51.8 W/cm².

Keywords: VO$_2$ film, heterojunction, phase transition threshold, infrared switching efficiency, laser-induced phase transition

1. Introduction

VO$_2$ is a typical phase-transition metal oxide [1] that exhibits a reversible phase transition under the external stimuli such as heat [1], electricity [2], and light [3], and has been widely investigated in the fields of materials science [4], physics [5], and electronics [6]. Below the phase transition threshold, VO$_2$ is in the monoclinic phase (*M*-phase), exhibiting the insulator or semiconductor properties, including a high resistivity, a high visible and an infrared transmittance, and a low reflectivity. Above the phase transition threshold, VO$_2$ transitions to the rutile phase (*R*-phase), exhibiting the metallic properties, including a low resistivity, a low infrared transmittance, and a high reflectivity [7]. This phenomenon is known as the insulator-to-metal transition (IMT) [8].

Despite the promising application prospects of VO$_2$ film in many fields such as the smart windows and the infrared detection [9], its high phase transition threshold still restricts its broader applications. In order to overcome this problem, the researchers have explored various methods to modulate the phase transition threshold of VO$_2$, such as the element doping [10], the interfacial strain [11], and the carrier injection [12].

The elemental doping is one of the most effective and simplest strategies to modulate the phase transition threshold of VO$_2$ [13]. The high-valent metal ions doping such as W^{6+}, Mo^{6+} etc., typically reduces the phase transition threshold of VO$_2$ [14], while the low-valent metal ions doping such as Ca^{2+}, Mg^{2+} etc., may increase the phase transition threshold [15]. However, generally the high-valent metal ions doping can inevitably degrade the optical properties of the VO$_2$ film and reduce its infrared switching efficiency (r). Although the low-valent metal ions doping can improve the optical properties and the r, it tends to increase the phase transition threshold. Hu et al. [16] reduced the thermotropic phase transition temperature (T_c) of VO$_2$ to 28 °C with W doping, but the infrared transmittance before the IMT (t_M) decreased by approximately 20%.

The lattice strain is another effective method to modulate the phase transition threshold of VO$_2$ [17]. The lattice mismatch between the substrate and the VO$_2$ film induces an internal stress within the film. Specifically, the application of tensile strain along the a- or b-axis or the compressive strain along the c-axis of the rutile phase decreases the phase transition threshold. Choi et al. [17] deposited the VO$_2$ films on various sapphire substrates and achieved the lowest T_c of 53.5 °C on the m-plane of sapphire. However, this method is still limited by the substrate materials and the film thickness. As the film thickness increases, the lattice strain gradually relaxes, weakening its effect on the modulation of the phase transition threshold.

The carrier injection is also another effective method to modulate the phase transition threshold of VO$_2$. The metal nanoarrays or the metal interlayers embedded in the VO$_2$ film provides extra free electrons, enhancing the conductivity and reducing the phase transition threshold [18]. However, the addition of metallic components also reduces the optical properties but provides a limited reduction of the phase transition threshold. Zhou et al. [12] embedded a periodic array of Ag nanoparticles into the VO$_2$ (M) film, reducing the T_c of the film to 57.5°C. However, the Ag nanoparticles not only provided extra free electrons to the VO$_2$ film, but also introduced additional light scattering and non-resonant absorption, leading to a decrease of the transmittance.

Overall, each of these methods has certain limitations, although they can effectively decrease the phase transition threshold of VO$_2$ film. The reduction of the phase transition threshold is often accompanied by a decrease for both the optical property and r. Therefore, it is crucial to develop a modulation method that can reduce the phase transition threshold of the VO$_2$ film while can maintain its optical property. To address this issue, the researchers have proposed the heterojunction structures based on VO$_2$ films [19]. Zhao et al. [19] fabricated the AZO layer on the VO$_2$ layer to form an n-AZO/n-VO$_2$ heterojunction, successfully reduced the T_c to 41.5°C, but also decreased the t_M to 44.0%. This is because the AZO layer provided additional free electrons to the VO$_2$, which lowered its T_c and infrared transmittance. However, as an anti-reflection layer, the AZO matched the refractive index of the VO$_2$ layer, thereby improved the visible light transmittance of the heterojunction.

TiO$_2$, a typical buffer layer, can enhance the transmittance of the insulator VO$_2$ film across the visible and infrared spectra through the interface strain [20]. Furthermore, as a wide-bandgap semiconductor, its free carriers concentration and conductivity can be improved via a doping of high-valent elements, such as Nb etc.[21] , thus it can provide additional carriers to the VO$_2$ film through an ohmic contact [22]. Nb: TiO$_2$ layer injected additional free electrons into the VO$_2$ layer in the VO$_2$/Nb: TiO$_2$ junction, not only reduced the phase transition threshold, but also improved the optical property of the VO$_2$ film [23,24]. However, the limited electron donation capacity of Nb^{5+} ions in the TiO$_2$ lattice resulted in only a modest reduction of the phase transition threshold in VO$_2$.

As a high-valent metal element, W doping can more effectively introduce additional free electrons into the TiO$_2$ film than Nb or Mo. W has one more valence electron than Nb, and the same number of valence electrons

as Mo. However, the lower 5d orbital energy level of W compared with the that of 4d orbital of Nb or Mo drives the formation of strongly ionic W–O bonds, promoting more electrons transfer to the TiO_2 lattice from W, showing a higher oxidation state for W confirmed by Bader charge analysis. Concurrently, the ionic bonding significantly reduces the oxygen vacancy formation energy, resulting in the formation of more oxygen vacancies and the release of more free electrons [25,26]. Therefore, W-doped TiO_2 film will have a greater potential to modulate the phase transition threshold of VO_2. Compared with the direct W doping for VO_2 film, the VO_2/W-TiO_2 heterojunction may not only effectively avoid the optical performance degradation, but also may improve the crystallization quality of the upper VO_2 layer via the TiO_2 layer, thereby enhancing its phase transition performance.

In this work, we constructed a VO_2/W-TiO_2 heterojunction via depositing a VO_2 layer on the W-doped TiO_2 layer covering K9 glass with RF magnetron sputtering and post annealing, to address the long-standing contradiction between the phase transition threshold and the optical property of VO_2 film. The effects of W doping concentration in the TiO_2 layer on the optical properties, the electrical properties, and the phase transition threshold of the heterojunction were investigated.

2.   Experimental process

Fabrication: The W-doped TiO_2 and VO_2 layers were sequentially deposited on K9 glass with the high-purity V_2O_5 and TiO_2 targets (99.99%, Nanchang Guocai Technology Co., Ltd.) via RF magnetron sputtering. The sputtering gas was argon (Ar, 99.999%), and the reactive gas was oxygen (O_2, 99.999%). W doping was performed through the placement of W pieces of different sizes on the TiO_2 target. For the TiO_2 film deposition, the O_2 and Ar flow rates were 4 sccm and 64 sccm, and the deposition thickness was 15 nm. For the V_2O_5 film deposition, the O_2 and Ar flow rates were 1.5 sccm and 60 sccm, respectively, and the deposition thickness was 30 nm. The background vacuum was 9×10^{-4} Pa, the sputtering pressure was 1 Pa, and the sputtering power was 200 W. The substrate temperature for the V_2O_5 film deposition was set to 500 °C, and the film thickness was controlled by the sputtering time. The V_2O_5/W-TiO_2 film was annealed at 570 °C for 90 minutes in an Ar atmosphere, with a heating rate of 6 °C/min and a furnace cooling afterward. Finally, the VO_2/W-TiO_2 composite film, the heterojunction, was obtained.

Characterization: The chemical composition of the film was analyzed with the EDAX spectrometer (EDAX, Crossbeam 550, Carl Zeiss). The phase component of the film was analyzed with the X-ray diffractometer (XRD, D8 Discover, Bruker AXS). The surface morphology of the film was observed with the FIB microscope (FIB, Crossbeam 550, Carl Zeiss). The thickness of the film was measured with the spectroscopic ellipsometer (COSE-D-VN-D-C-AF-MR-T, Syscos). The electrical property of the film was measured with the Hall effect measurement system (ezHEMS, Nanomagnetics). The transmittance spectrum of the film in the wavelength range of 350–2500 nm and the transmittance-temperature hysteresis curve at 2500 nm were recorded with a UV-Vis-NIR spectrophotometer (UH4150, Hitachi). The laser-induced phase transition performance of the film at a wavelength of 1993 nm was tested with a Tm: YAP solid-state laser [27].

3.   Results and discussion

3.1 The W doping concentration of W-TiO2 layer

The EDS spectra for the W-TiO_2 layer of the heterojunction are shown in Figure 1. The W doping

concentration was analyzed through the EDS spectra, and the weight percentage (wt%) of W^{6+} doped in TiO_2 was converted to the atomic percentage (at%) with the Formula 1.

$$at\%_i = \frac{\frac{wt\%_i}{M_i}}{\sum_j \frac{wt\%_j}{M_j}} \times 100 \qquad (1)$$

Where M is the atomic mass of the element. The W doping concentrations were calculated as 1.01 at%, 1.37 at%, 1.66 at%, 2.05 at%, and 2.46 at%.
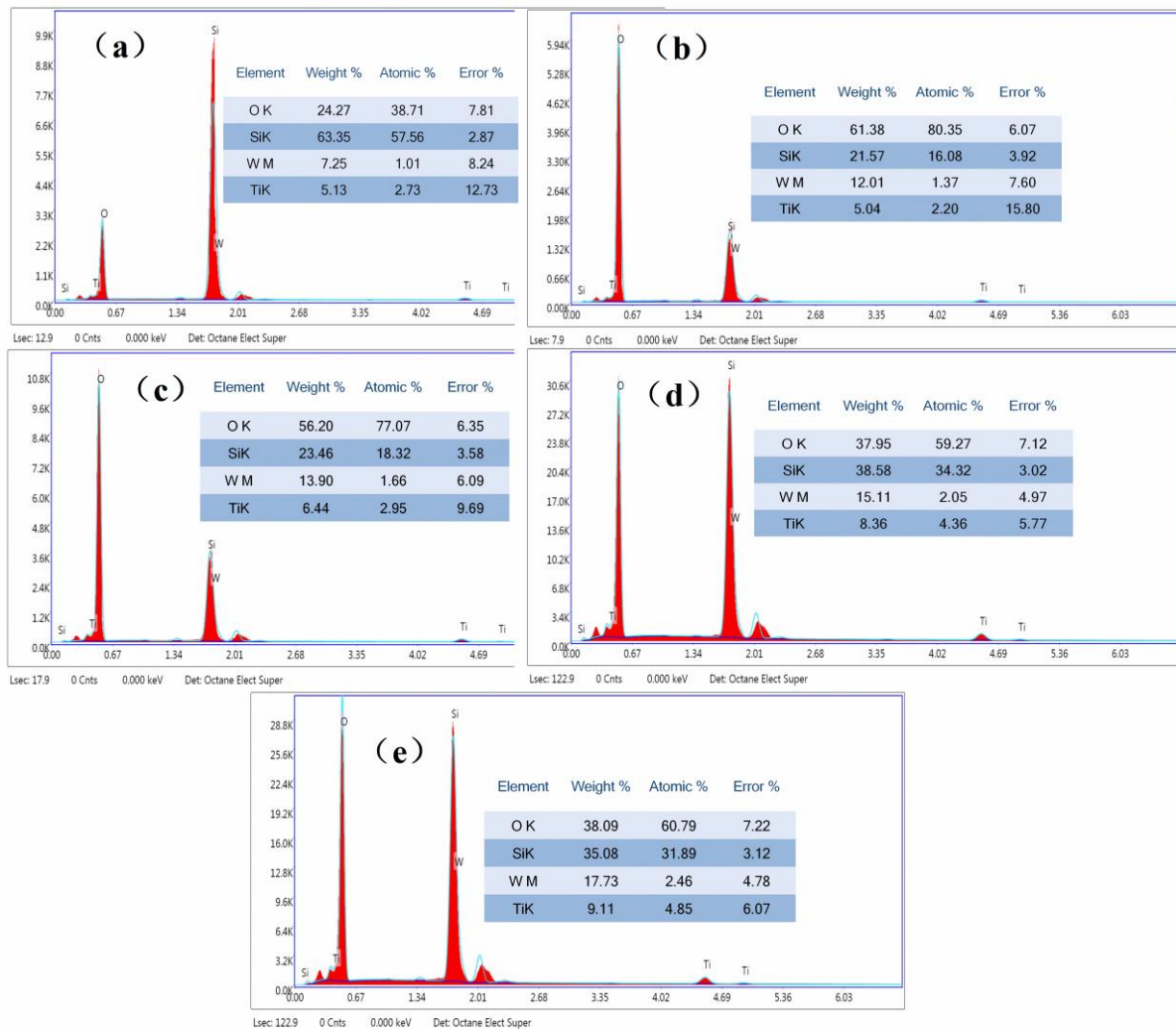

Figure 1. The EDS spectra for the W-TiO_2 layer of the heterojunction: (a) 1.01 at%; (b) 1.37 at%; (c) 1.66 at%; (d) 2.05 at%; (e) 2.46 at%

3.2 The effect of W doping concentration on the phase crystal structures of the VO2/W-TiO2 n-n heterojunction

The effect of W doping concentration on the phase crystal structures of the heterojunction is shown in Figure 2. The diffraction peaks corresponding to TiO_2 and VO_2 crystals appear at $2\theta = 25.3°$ and $27.8°$, respectively. Compared with the PDF cards 21-1272# for the TiO_2 anatase phase and 43-1051# for the VO_2 monoclinic phase, these peaks correspond to the TiO_2 (101) and the VO_2 (011) crystal planes, respectively.

The absence of any additional peak in the pattern indicates the high purity of the prepared film. After a careful

observation, we can notice that as the W doping concentration increases, the diffraction peak of the TiO_2 (101) crystal plane shifts to the right a little. This is because the incorporation of W^{6+} enhances the covalency of W-O bonds and shortens them through the hybridization with O_{2p} orbitals, leading to a reduction of the interplanar spacing. Meanwhile, the charge compensation through the oxygen vacancy formation during W^{6+} doping can induce local lattice contraction, which further shortens the W-O bonds. In addition, the ionic radius of W^{6+} is 0.60 Å, which is slightly smaller than that of Ti^{4+} (0.605 Å) [28,29].

The displacement of the peak positions is strongly correlated with the change of the interplanar spacing. According to the Bragg's formula, $2dsin\theta = n\lambda$, where d is the interplanar spacing, θ is the diffraction angle, n is the diffraction order, and λ is the X-ray wavelength. It can be seen that the W doping leads to a decrease in the interplanar spacing of TiO_2, and the diffraction peak shifts to the right slightly.

The diffraction peak of the VO_2 (011) shows no significant shift, because the VO_2 (R) crystal tends to grow preferentially along the (110) crystal plane, which has a lower surface energy, during the growth process. During the annealing process, the VO_2 nanoparticles undergo surface migration, allowing some VO_2 lattices to break free from the constraint of the underlying TiO_2. They preferentially grow along the direction that minimizes the sum of the surface energy, the interface energy, and the strain energy, which is the $VO_2(R)$ (110) crystal plane. After being cooled to room temperature, it transforms into the $VO_2(M)$ (011) crystal plane.
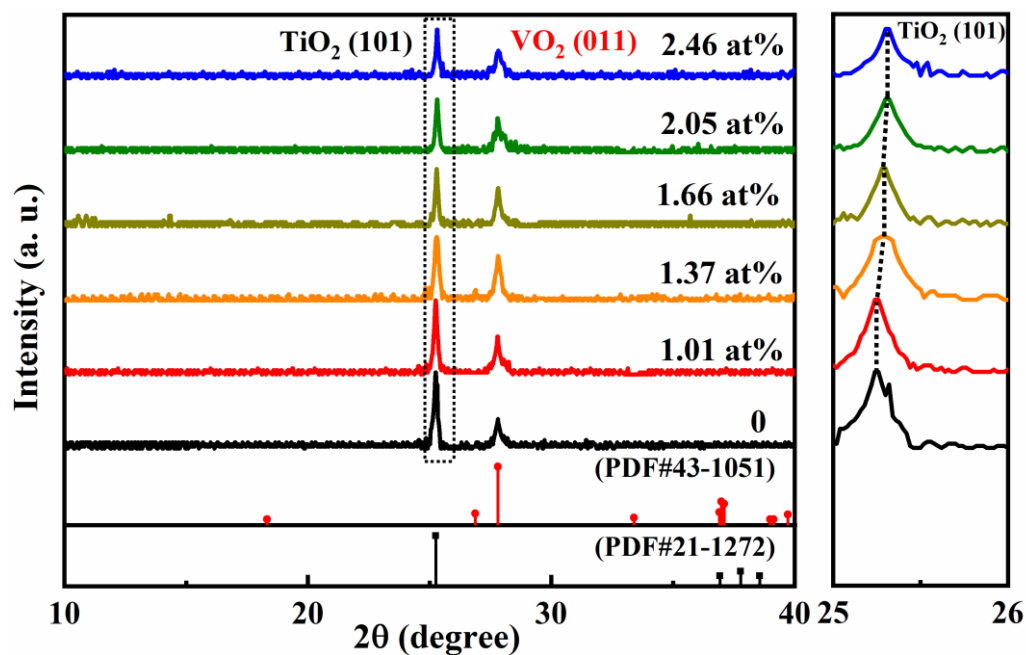

Figure 2. The XRD patterns of the VO_2/W-TiO_2 heterojunctions

The grain sizes D for both the TiO_2 and the VO_2 layers were calculated according to the Scherrer formula: $D = k\lambda/\beta cos\theta$ (where k is the Scherrer constant (0.89), and β is the full width at half maximum of the diffraction peak). The characteristic parameters of the diffraction peaks and the grain sizes for the VO_2/W-TiO_2 heterojunction are listed in Table 1.

Table 1. The characteristic parameters of the diffraction peaks and grain sizes of the VO_2/W-TiO_2 heterojunctions

W doping (at%)	TiO$_2$			VO$_2$		
	β (°)	2θ (°)	D (nm)	β (°)	2θ (°)	D (nm)
0	0.155	25.27	51.92	0.243	27.79	33.41
1.01	0.158	25.27	50.94	0.241	27.80	33.57
1.37	0.160	25.28	50.30	0.222	27.80	36.44
1.66	0.162	25.29	49.68	0.238	27.81	33.99
2.05	0.168	25.30	47.91	0.245	27.81	33.02
2.46	0.180	25.31	44.71	0.246	27.81	32.89

3.3 The effect of W doping concentration on the surface morphology of the VO2/W-TiO2 n-n heterojunction

The effect of W doping concentration on the surface morphology of the VO_2/W-TiO_2 heterojunction is shown in Figure 3.
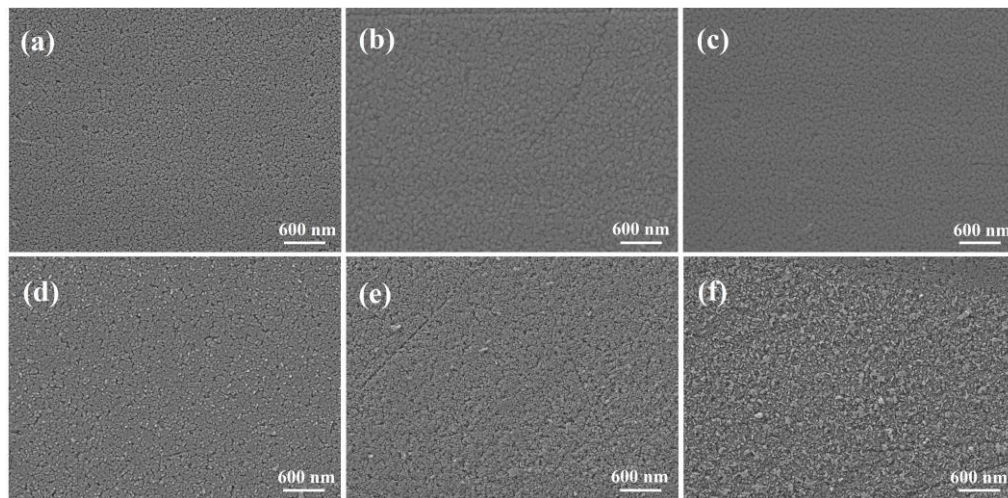

Figure 3. The effect of W doping concentration on the surface morphology of the VO_2/W-TiO_2 *n-n* heterojunction: (a) 0 at%; (b) 1.01 at%; (c) 1.37 at%; (d) 1.66 at%; (e) 2.05 at%; (f) 2.46 at%

When the W doping concentration is 0, the VO_2 particles are relatively large, and their irregular shapes lead to a loosely packed arrangement with noticeable gaps and some holes, as shown in Figure 3(a). As the W doping concentration increases to 1.01 at%, the VO_2 particles become more compact, the gaps gradually decrease, but some cracks still remain in the film, as shown in Figure 3(b). When the W doping concentration further increases to 1.37 at%, the film presents a uniform particle distribution and a smooth surface as shown in Figure 3(c). That is, the film is rather uniform and compact. However, with the excessive W doping, the surface of the VO_2 film becomes uneven and increasingly rough, and the strong agglomeration occurs, please see Figure 3(d) to 3(f).

3.4 The effect of W doping concentration on the electrical properties of the VO2/W-TiO2 n-n heterojunction

The effect of W doping concentration on the electrical properties of the VO_2/W-TiO_2 heterojunction is shown in Figure 4. As the W doping concentration increases, the carrier concentration (n) rises from 2.5×10^{19} cm^{-3} to 2.2×10^{21} cm^{-3}, increasing by about two orders of magnitude. This phenomenon is attributed to the introduction of a large number of additional free electrons with W doping. The n gradient at the heterojunction interface drives electrons to migrate from the W-TiO_2 layer to the VO_2 layer, significantly increasing the n of the VO_2 layer.

The carrier mobility (μ) first increases and then decreases, with a relatively minor variation compared with the n, which increases from 0.212 cm$^2 \cdot$v$^{-1} \cdot$s^{-1} to 0.255 cm$^2 \cdot$v$^{-1} \cdot$s^{-1}, and then decreases to 0.191 cm$^2 \cdot$v$^{-1} \cdot$s^{-1}. When the W doping concentration is 1.37 at%, the μ reaches its maximum value. This is attributed to the largest grain size, and the densest surface of the film, both of which effectively reduce the carrier scattering of the heterojunction. As the W doping concentration continues to increase, the μ gradually decreases. This is because that the excessive W doping increases the grain boundaries of the TiO_2 layer, making the film surface rougher and generating more defects and scattering centers, ultimately restricting the free movement of carriers [30].

According to the formula $\rho = 1/nq\mu$ (where q is the charge of the carriers, 1.6×10^{-19} C), the resistivity (ρ) first decreases and then increases, and finally stabilizes. The n at 0 at% W doping is two orders of magnitude lower than that at other doping levels, resulting in a two-order-magnitude difference of ρ, which decreases from a maximum value of 1.18 $\Omega \cdot$cm to a minimum value of 1.44×10^{-2} $\Omega \cdot$cm. This significant change indicates that W doping can effectively improve the conductivity of the TiO_2 layer, thereby enhancing the conductivity of the VO_2/W-TiO_2 heterojunction.
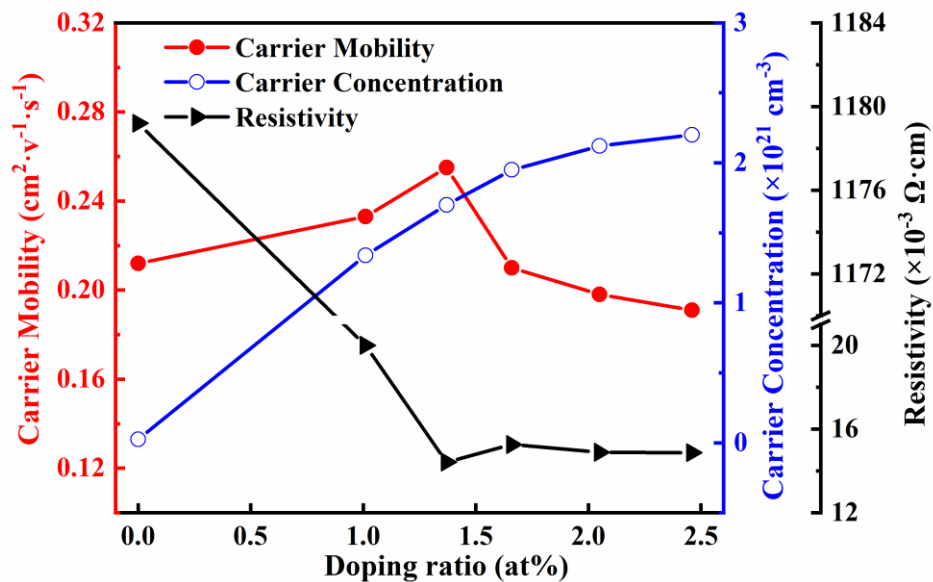

Figure 4. The effect of W doping concentration on the electrical properties of the VO_2/W-TiO_2 *n-n* heterojunction

3.5 The effect of W doping concentration on the phase transition performance of the VO2/W-TiO2 n-n heterojunction

The effect of W doping concentration on the thermotropic phase transition performance of the VO_2/W-TiO_2 heterojunction is shown in Figure 5. As shown in Figure 5(a), all the transmittance spectra for the VO_2/W-TiO_2

heterojunctions in the wavelength range of 350-2500 nm show a distinct IMT characteristic. As the W doping concentration increases, the transmittance of the heterojunction at 2500 nm gradually decreases before the phase transition, and the decreasing amplitude gradually increases, as shown by the blue polyline in Figure 5(d).

The hysteresis curve and its first-order derivative curve at 2500 nm for the heterojunction are shown in Figures 5(b) and 5(c), respectively, and the phase transition performance parameters are summarized in Table 2.

VO$_2$ film exhibits a pronounced thermal hysteresis during the phase transition, in which two distinct transition thresholds are observed during the heating and cooling processes, respectively, forming a characteristic hysteresis loop. Therefore, to more accurately characterize the phase transition behavior, the T_c in this work is defined as the midpoint between the minimum points of the curves during heating and cooling, as shown in Formula (2). And the positions for T_c were marked with the straight lines in Figure 5(b), respectively.

$$Tc = \frac{T_{heat} + T_{cool}}{2} \tag{2}$$

The results indicate that as the W doping concentration rises from 0 to 1.37 at%, the T_c significantly decreases from 67.9 °C to 54.3 °C. As the W doping concentration continues to increase, the T_c instead rises and stabilizes at approximately 58°C. When the W doping concentration reaches 1.37 at%, the heterojunction exhibits the lowest T_c, as shown by the red polyline in Figure 5(d).

When the W doping concentration increases from 0 to 1.37 at%, both the t_M and the infrared transmittance after the phase transition (t_R) slightly decrease. The value of r, calculated as $r = (t_M - t_R)/t_M$, increases from 53.6% to 56.8%, with a corresponding increase of 3.2%. The width of the hysteresis curve (ΔT) is 10.8 °C. With a further increase of the W doping concentration, both the t_M and the t_R exhibit a significant decrease, the r first rises to a peak value of 58.5% and then declines, while the t_M stabilizes at around 58 °C.
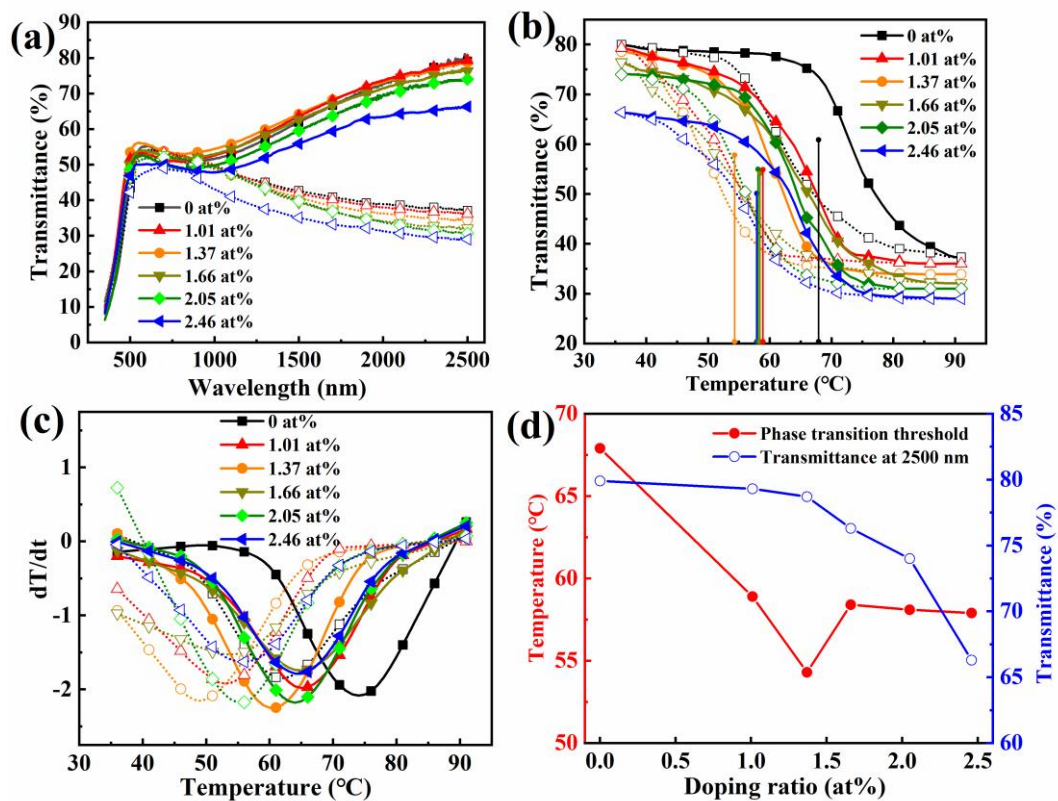

Figure 5. The effect of W doping concentration on the thermotropic phase transition performance of the VO$_2$/W-TiO$_2$ heterojunction:

(a) The transmittance spectra of the VO$_2$/W-TiO$_2$ heterojunction in the wavelength range of 350-2500 nm. (b) The hysteresis curves of the transmittance at 2500 nm of the VO$_2$/W-TiO$_2$ heterojunction during heating and cooling processes. (c) The first-order derivative curves of the hysteresis curves in Figure (b). (d) The effect of W doping concentration on the T_c and t_M of the VO$_2$/W-TiO$_2$ heterojunction.

In Figure (a), the solid lines represent the curves of the heterojunction before the phase transition, and the dashed lines represent the curves after the phase transition; in Figures (b) and (c), the solid and dashed lines correspond to the heating and cooling processes, respectively.

In particular, when the W doping concentration is 1.37 at%, the thermotropic phase transition performance of the heterojunction is the best. The T_c reaches its minimum value of 54.3 °C, the maximum visible light transmittance (infrared transmittance) reaches its highest value of 56.2%, the t_M is 78.7%, and the r is 56.8%.

The effect of laser power density on the transmittance of the VO$_2$/W-TiO$_2$ heterojunction at 1993 nm, along with its first-order derivative curve, is shown in Figure 6. As the W doping concentration increases, the laser-induced and the thermotropic phase transition performances of the heterojunction exhibit similar trends. It is worth noting that during the laser-induced phase transition process, the hysteresis curve of VO$_2$ is steeper. This implies that the response time of the laser-induced phase transition is shorter, the phase transition is faster, more stable, and can be regarded as nearly instantaneous.

Table 2. The thermotropic phase transition performance parameters of the VO$_2$/W-TiO$_2$ *n-n* heterojunction

W doping (at%)	T_c (°C)	ΔT (°C)	t_M (%)	t_R (%)	r (%)	$t_{vis\text{-}max}$ (%)
0	67.9	12.0	79.9	37.1	53.6	51.5
1.01	58.9	11.8	79.3	36.1	54.5	53.5
1.37	54.3	10.8	78.7	34.0	56.8	56.2
1.66	58.4	10.5	76.3	32.1	57.9	54.0
2.05	58.1	9.8	74.0	30.7	58.5	52.6
2.46	57.9	9.5	66.3	29.0	56.3	50.2

In order to analyze the effect of W doping on the laser-induced phase transition of the heterojunction, the relevant data from Figure 6 are summarized in Table 3. As the W doping concentration increases, the laser-induced phase transition threshold (P_c) of the heterojunction first decreases, and then increases and remains relatively stable, which is similar to T_c. When the W doping concentration is 1.37 at%, the P_c reaches its lowest value of 51.8 W/cm², the t_M is 73.0%, and the r is 50.8%. Compared with the undoped heterojunction, the P_c decreased by 19.5 W/cm², and the r increased by 2.5%.
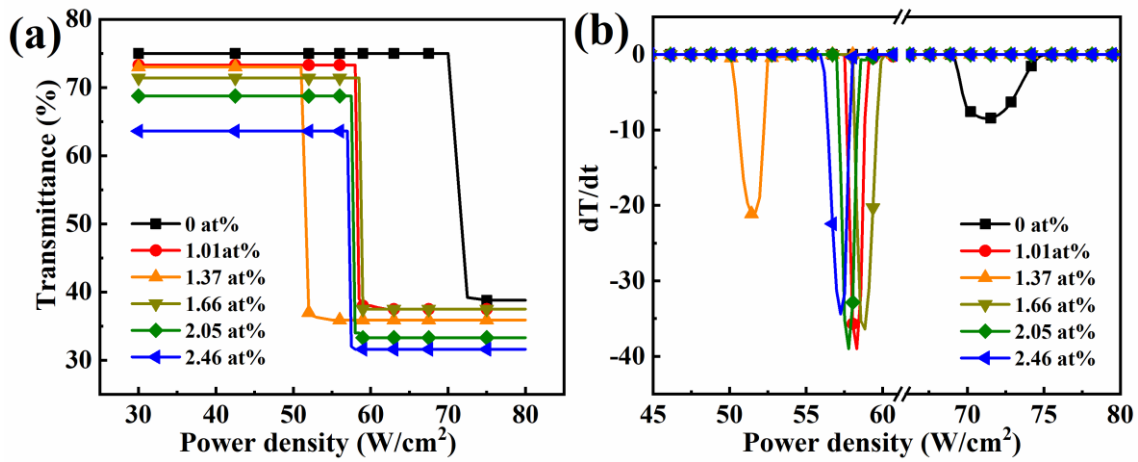
Figure 6. The effect of W doping concentration on the laser-induced phase transition performance of the VO$_2$/W-TiO$_2$ *n-n* heterojunction: (a) The variation of the transmittance of the VO$_2$/W-TiO$_2$ heterojunction at 1993 nm. (b) The first-order derivative curves of the Figure (a)

To explain the above experimental results, the optical bandgap (E_g) of the heterojunction was calculated based on the Tauc formula (3) and the absorption coefficient formula (4), based on the curves in the Figure 7:

$$\alpha h v = A(h v - E_g)^2 \tag{3}$$

$$\alpha = -\frac{1}{d}\ln T \tag{4}$$

Here, the α is the absorption coefficient, the d is the thickness of the heterojunction, the T is the transmittance, the $h v$ is the photon energy, the h is Planck's constant, and the A is a constant. The optical bandgap (E_g) of the material is determined by the intersection of the extrapolated linear region of the curve in the figure with the X-axis.

Table 3. The laser-induced phase transition performance parameters of the VO$_2$/W-TiO$_2$ *n-n* heterojunction

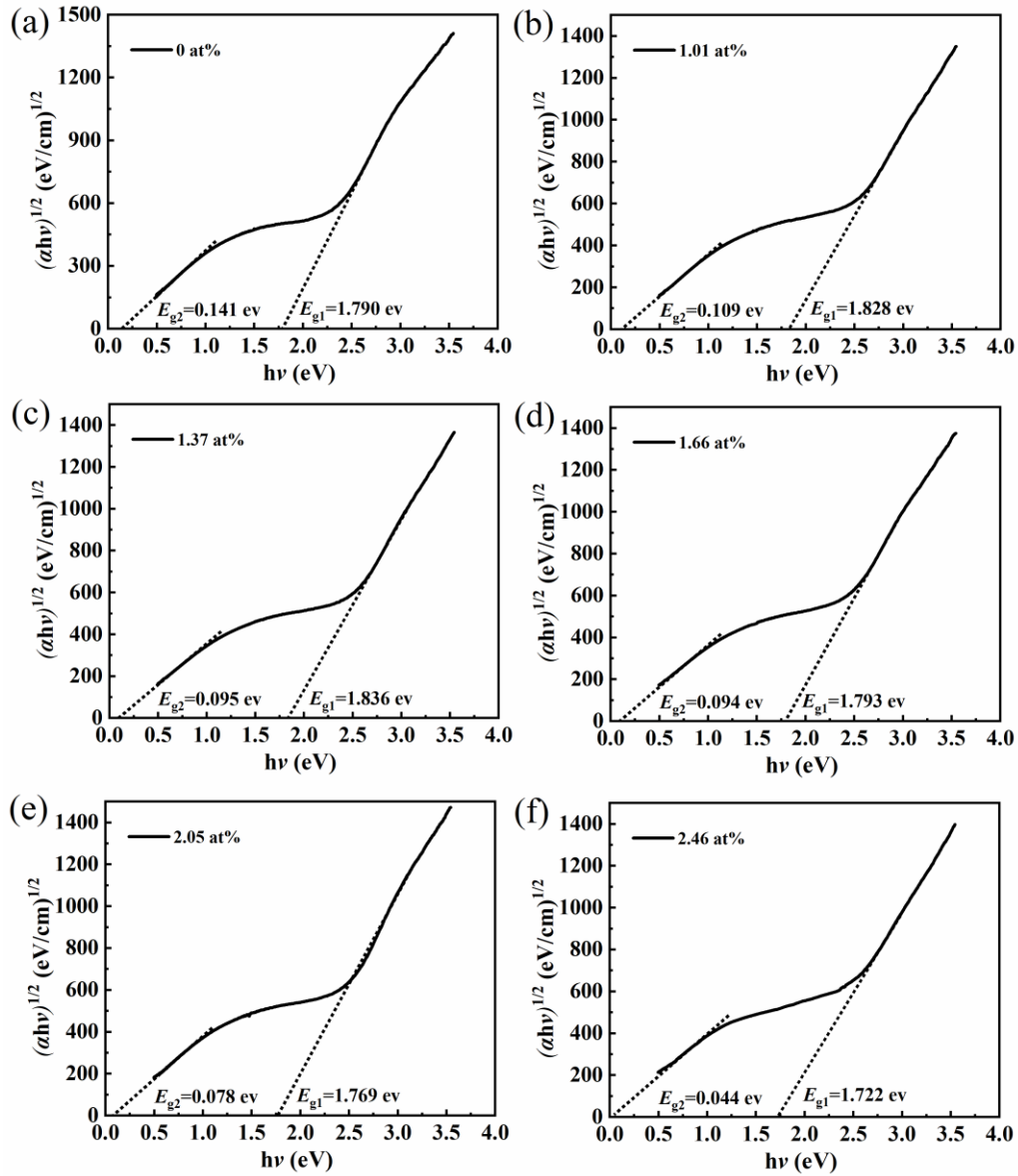| W doping (at%)	P_c (W/cm^2)	t_M (%)	t_R (%)	r (%)
0	71.3	75.0	38.8	48.3
1.01	58.3	73.3	37.5	48.8
1.37	51.8	73.0	35.9	50.8
1.66	58.8	71.4	37.5	47.5
2.05	57.8	68.8	33.3	51.6
2.46	57.2	63.6	31.6	50.3

Figure 7. The Tauc plot of the VO_2/W-TiO_2 *n-n* heterojunction: (a) 0 at%; (b) 1.01 at%; (c) 1.37 at%; (d) 1.66 at%; (e) 2.05 at%; (f) 2.46 at%

From the figure 7, it can be observed that the optical bandgap can be divided into a high-energy bandgap E_{g1} and a low-energy bandgap E_{g2}, which correspond to the direct bandgap and the indirect bandgap of VO_2, respectively [31]. Based on the molecular orbital and crystal field theory model of VO_2 proposed by Goodenough, as well as the subsequent researches, the electronic transitions related to these bandgaps are further differentiated [32]. Among them, E_{g1} dominates the transmittance characteristic of the visible light range, while E_{g2} is related to the IMT [33].

As the W doping concentration increases, it can be observed that the trend of E_{g1} of the heterojunction is similar to that of the $t_{vis-max}$, The E_{g1} reaches its maximum when the W doping concentration is 1.37 at%. Meanwhile, as the doping concentration increases, the E_{g2} gradually decreases, which is consistent with the trend of the t_M of the heterojunction. Comparing with the change of the n shown in Figure 4, it can be observed that the increase of the n reduces the E_{g2} bandgap. The decrease of the bandgap lowers the energy required for the electronic transitions, which in turn reduces the phase transition threshold of the heterojunction [34].

During the laser-induced phase transition, the laser excitation promotes the electrons from the valence band to the conduction band, generating a large number of free electrons, which leads to an increase of the n. When the n reaches a critical value, VO$_2$ undergoes the IMT, and the process can be regarded as an instantaneous phase transition. Based on Mott theory [19,35], the n is the key parameter to control the IMT. When n exceeds the Mott critical value, the Coulomb interaction between the electrons is effectively screened, the localization effect disappears, and the system transitions from an insulating state to a metallic state.

As the W doping concentration increases from 0 to 1.37 at%, both the n and μ of the TiO$_2$ layer are significantly improved. More carriers are injected into the VO$_2$ layer, driven by the carrier concentration gradient, thereby increasing the n of VO$_2$. Therefore, the increase of W doping concentration of the TiO$_2$ layer leads to a decrease of both the T_c and P_c of VO$_2$. In addition, the increase of n rises the Fermi level, narrowing the E_{g2} and consequently reducing the optical transmittance [19].

As the W doping concentration increases, the n continues to rise, but the excessive doping can induce the lattice distortion of the TiO$_2$ layer, leading to the formation of defects. Furthermore, the defects serve as the additional electron scattering centers, restricting the migration of carriers from the TiO$_2$ layer to the VO$_2$ layer, leading to the increase of both T_c and P_c, as shown in Figure 4.

Meanwhile, the continued rise of n further narrows the optical bandgap. Moreover, the deterioration of the surface morphology of the film increases the grain boundary scattering, leading to a significant drop of both t_M and t_R.

To better highlight the novelty of this work, the heterojunction with a W doping concentration of 1.37 at% is compared with W-doped VO$_2$ film, as shown in Figure 8. To avoid the influence of other factors, the W-doped VO$_2$ film was prepared under the same conditions. We precisely controlled the W doping concentration in W-doped VO$_2$ film, regulated its T_c to approximately 54 °C, very close to that of the heterojunction. We can see that, both the t_M and t_R of the heterojunction exhibit approximately an 8% enhancement compared with the W-doped VO$_2$ film.
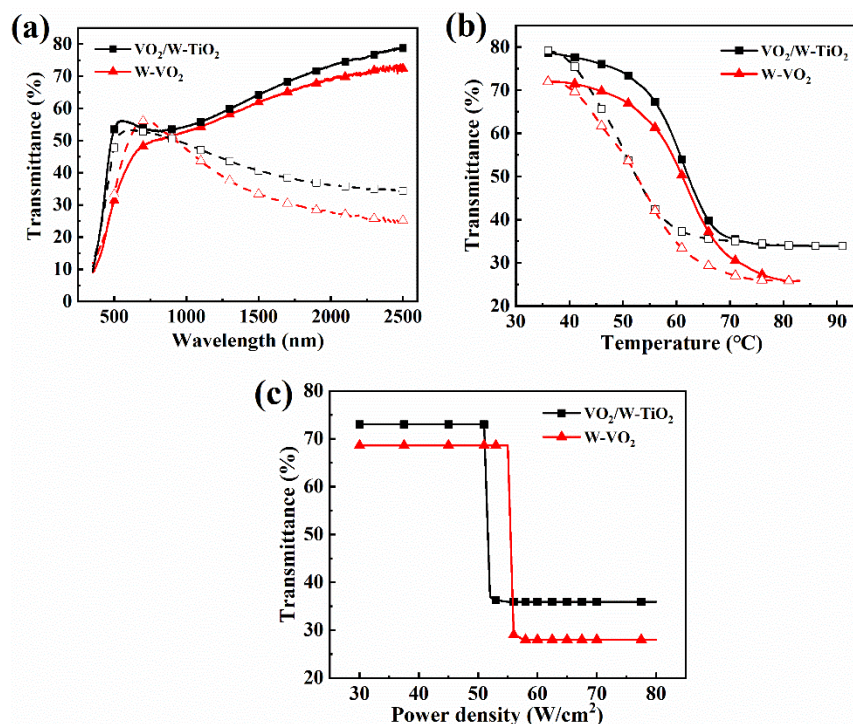

Figure 8. The comparison of phase transition performance between the VO$_2$/W-TiO$_2$ heterojunction and W-doped VO$_2$ film: (a) The

transmittance spectra within 350-2500 nm. (b) The hysteresis curves of the transmittance at 2500 nm during heating and cooling processes.

(c) The variation of the transmittance at 1993 nm

3.6 The quality factor of the VO2/W-TiO2 n-n heterojunction

In order to comprehensively evaluate the phase transition performance of the VO_2/W-TiO_2 heterojunction, this work refers to the laser protection performance quality factor ($QOLP$) established by Zhao et al. [36], with the following formulas:

$$QOLP = \frac{t_{low-p}{}^a}{P_c{}^b \cdot P_e{}^c} \times 10^n \qquad (5)$$

Where the $t_{low\text{-}p}$ is the transmittance of the M phase heterojunction at the low-power laser, the P_c is the critical laser power density for the heterojunction to complete the IMT, and the P_e is the output power density of the laser passing through the R-phase heterojunction. The exponents a, b, c, and n are 1, 2, 2, and 6, respectively.

According to the formula (5), the $QOLP$ of the VO_2/W-TiO_2 heterojunction was calculated, and the result are shown in the Figure 9. It can be seen that the $QOLP$ reaches its maximum value when the W doping concentration is 1.37 at%, which is 0.79 $(W/cm^2)^{-4}$, more than four times of that of the undoped one, 0.19$(W/cm^2)^{-4}$. This heterojunction exhibits the best comprehensive laser protection performance.
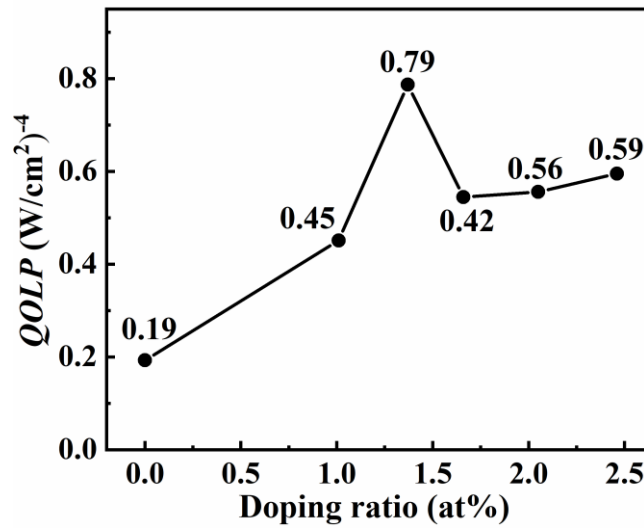

Figure 9. The $QOLP$ of the VO_2/W-TiO_2 *n-n* heterojunction

4. Conclusion

This work prepared VO_2/W-TiO_2 *n-n* heterojunctions on K9 glass substrates with magnetron sputtering, and focused on the effects of the W doping for the TiO_2 layer on the phase transition properties of the heterojunction.

As the W doping concentration increases, T_c of the heterojunction first decreases and then increases a little, while its P_c first increases and then decreases. When the W doping concentration is 1.37 at%, the heterojunction exhibits the best comprehensive performance, its r is up to 56.8%, while its T_c decreases to 67.9 °C, its P_c 51.8 W/cm^2. And its laser protection performance quality factor reaches 0.79 $(W/cm^2)^{-4}$, which is 4 times that of the undoped heterojunction. This improvement is mainly due to the injection of carriers from the W-TiO_2 layer into the VO_2 layer, weakening the electron-electron interactions.

Credit authorship contribution statement

Weizheng Shi: Writing - original draft, Methodology, Investigation, Formal analysis, Conceptualization. Leran Zhao: Methodology, Investigation. Qiujing Xu: Investigation. Yushan Zheng: Investigation. Juncheng Liu: Supervision, Resources, Project administration, Funding acquisition.

Data availability

The data that support the findings of this study are available from the corresponding author upon a reasonable request.

Conflict of Interest

There is no conflict of interest for this study.

Reference

[1] Zhou X, Ping Y, Gao J, Gu D, Zhou H, Yang M, Jiang Y, Facile fabrication of HfO_2/nanocomposite vanadium oxide bilayer film with enhanced thermochromic properties and excellent durability, Applied Surface Science 597 (2022) https://10.1016/j.apsusc.2022.153729.

[2] Kaydashev V, Khlebtsov B, Kutepov M, Nikolskiy A, Kozakov A, Konstantinov A, Mikheykin A, Karapetyan G, Kaidashev E, Photothermal Effect and Phase Transition in VO_2 Enhanced by Plasmonic Particles, Materials 16 (2023) https://10.3390/ma16072579.

[3] Mogunov I A, Lysenko S, Fedianin A E, Kent A J, Akimov A V, Kalashnikova A M, A role of a picosecond strain in an ultrafast optically-driven phase transition in VO_2 nanostructures, Journal of Physics: Conference Series 1461 (2020) https://10.1088/1742-6596/1461/1/012108.

[4] Wu B, Zhang D, Wang C, Zhang K, Wu X, Transparent spacecraft smart thermal control device based on VO_2 and hyperbolic metamaterials, Physical Chemistry Chemical Physics 25 (2023) 20302-20307. https://10.1039/d3cp00913k.

[5] Dönges S A, Khatib O, O'callahan B T, Atkin J M, Park J H, Cobden D, Raschke M B, Ultrafast Nanoimaging of the Photoinduced Phase Transition Dynamics in VO_2, Nano Letters 16 (2016) 3029-3035. https://10.1021/acs.nanolett.5b05313.

[6] Cui Y, Ke Y, Liu C, Chen Z, Wang N, Zhang L, Zhou Y, Wang S, Gao Y, Long Y, Thermochromic VO_2 for Energy-Efficient Smart Windows, Joule 2 (2018) 1707-1746. https://10.1016/j.joule.2018.06.018.

[7] Liang J, Fan Y, Su T, Wang S, Yu X, Research of Optical Performance of VO_2/V_2O_5 Composite Film with Ultra-High Luminous Transmittance, ECS Journal of Solid State Science and Technology 9 (2020) https://10.1149/2162-8777/abc1f3.

[8] Xu J, Chen D, Meng S, Decoupled ultrafast electronic and structural phase transitions in photoexcited

monoclinic VO$_2$, Science Advances 8 (2022) https://10.1126/sciadv.add2392.

[9] Li Z, Cao C, Li M, Wang L, Zhu D, Xu F, Huang A, Jin P, Yu L, Cao X, Gradient Variation Oxygen-Content Vanadium–Oxygen Composite Films with Enhanced Crystallinity and Excellent Durability for Smart Windows, ACS Applied Materials & Interfaces 15 (2023) 9401-9411. https://10.1021/acsami.2c21188.

[10] Hajlaoui T, Émond N, Quirouette C, Le Drogoff B, Margot J, Chaker M, Metal–insulator transition temperature of boron-doped VO$_2$ thin films grown by reactive pulsed laser deposition, Scripta Materialia 177 (2020) 32-37. https://10.1016/j.scriptamat.2019.09.019.

[11] Fan L L, Chen S, Liao G M, Chen Y L, Ren H, Zou C W, Comprehensive studies of interfacial strain and oxygen vacancy on metal–insulator transition of VO$_2$ film, Journal of Physics: Condensed Matter 28 (2016) https://10.1088/0953-8984/28/25/255002.

[12] Zhou Z, Li J, Xiong Z, Cao L, Fu Y, Gao Z, Reducing transition temperature and diluting brown-yellow color of VO$_2$ films via embedding Ag particles periodic arrays, Solar Energy Materials and Solar Cells 206 (2020) https://10.1016/j.solmat.2019.110303.

[13] Ivanov A V, Tatarenko A Y, Gorodetsky A A, Makarevich O N, Navarro-Cía M, Makarevich A M, Kaul A R, Eliseev A A, Boytsova O V, Fabrication of Epitaxial W-Doped VO$_2$ Nanostructured Films for Terahertz Modulation Using the Solvothermal Process, ACS Applied Nano Materials 4 (2021) 10592-10600. https://10.1021/acsanm.1c02081.

[14] Zong H, Chen H, Bian L, Sun B, Yin Y, Zhang C, Qiao W, Yan L, Hu Q, Li M, An approach for obtaining thermochromic smart windows with excellent performance and low phase transition temperature based on VO$_2$/tungsten-doped VO$_2$/VO$_2$ composite structure, Infrared Physics & Technology 137 (2024) https://10.1016/j.infrared.2024.105186.

[15] Panagopoulou M, Gagaoudakis E, Boukos N, Aperathitis E, Kiriakidis G, Tsoukalas D, Raptis Y S, Thermochromic performance of Mg-doped VO$_2$ thin films on functional substrates for glazing applications, Solar Energy Materials and Solar Cells 157 (2016) 1004-1010. https://10.1016/j.solmat.2016.08.021.

[16] Hu L, Tao H, Chen G, Pan R, Wan M, Xiong D, Zhao X, Porous W-doped VO$_2$ films with simultaneously enhanced visible transparency and thermochromic properties, Journal of Sol-Gel Science and Technology 77 (2015) 85-93. https://10.1007/s10971-015-3832-z.

[17] Choi Y, Lee D, Song S, Kim J, Ju T S, Kim H, Kim J, Yoon S, Kim Y, Phan T B, Bae J S, Park S, Correlation between Symmetry and Phase Transition Temperature of VO$_2$ Films Deposited on Al$_2$O$_3$ Substrates with Various Orientations, Advanced Electronic Materials 7 (2021) https://10.1002/aelm.202000874.

[18] Stefanovich G, Pergament A, Stefanovich D, Electrical switching and Mott transition in VO$_2$, Journal of Physics: Condensed Matter 12 (2000) 8837-8845. https://10.1088/0953-8984/12/41/310.

[19] Zhao L, Liu R, Ma J, Zhu H, Feng M, Liu J, Continuous modulation of VO$_2$ film's phase transition threshold and transmittance via n-AZO/n-VO$_2$ heterojunction, Applied Surface Science 655 (2024) https://10.1016/j.apsusc.2024.159545.

[20] Zhang D, Yang K, Li Y, Liu Y, Zhu M, Zhong A, Cai X, Fan P, Lv W, Employing TiO$_2$ buffer layer to improve VO2 film phase transition performance and infrared solar energy modulation ability, Journal of Alloys and Compounds 684 (2016) 719-725. https://10.1016/j.jallcom.2016.05.233.

[21] Yadav P V K, Ajitha B, Ahmed C M A, Reddy Y a K, Minnam Reddy V R, Superior UV photodetector performance of TiO$_2$ films using Nb doping, Journal of Physics and Chemistry of Solids 160 (2022)

https://10.1016/j.jpcs.2021.110350.

[22] Hiroi Z, Yamauchi T, Muraoka Y, Muramatsu T, Yamaura J-I, Efficiency of Photocarrier Injection in a VO_2/TiO_2:Nb Heterostructure, Journal of the Physical Society of Japan 72 (2003) 3049-3052. https://10.1143/jpsj.72.3049.

[23] Yang Y, Wang G, Huang W, Wang C, Yao Y, Mao X, Lin H, Zhang T, Qiu H, Li Z, Zhang H, Yin Y, Guo J, Guan Y, Yan W, Luo Z, Zou C, Tian Y, Xiao G, Li X, Gao C, Reversible optical control of the metal-insulator transition across the epitaxial heterointerface of a VO_2/Nb:TiO_2 junction, Science China Materials 64 (2021) 1687-1702. https://10.1007/s40843-020-1576-3.

[24] Madaras S E, Creeden J A, Lahneman D J, Harbick A, Beringer D B, Qazilbash M M, Novikova I, Lukaszew R A, Dynamics of the blue pump-induced ultrafast insulator-to-metal transition and relaxation in VO_2/TiO_2 and VO_2/TiO_2:Nb thin films, Optical Materials Express 10 (2020) https://10.1364/ome.394653.

[25] Azmat M, Haibo J, Naseem K, Ling C, Li J, A comparative study uncovering the different effect of Nb, Mo and W dopants on phase transition of vanadium dioxide, Journal of Physics and Chemistry of Solids 180 (2023) https://10.1016/j.jpcs.2023.111439.

[26] Sun C, Yan L, Yue B, Liu H, Gao Y, The modulation of metal–insulator transition temperature of vanadium dioxide: a density functional theory study, J. Mater. Chem. C 2 (2014) 9283-9293. https://10.1039/c4tc00778f.

[27] Ma J, Ou W, Zhao L, Shi W, Zhu H, Liu J, Effect of SiO_2 monocrystalline substrate orientation on the crystal structure and properties of VO_2 film, Journal of Alloys and Compounds 1010 (2025) https://10.1016/j.jallcom.2024.177968.

[28] Corbel G, Laligant Y, Goutenoire F, Suard E, Lacorre P, Effects of Partial Substitution of Mo^{6+} by Cr^{6+} and W^{6+} on the Crystal Structure of the Fast Oxide-Ion Conductor Structural Effects of W^{6+}, Chemistry of Materials 17 (2005) 5390-5390. https://10.1021/cm0599969.

[29] Xiao Y, Cheng N, Kondamareddy K K, Wang C, Liu P, Guo S, Zhao X-Z, W-doped TiO_2 mesoporous electron transport layer for efficient hole transport material free perovskite solar cells employing carbon counter electrodes, Journal of Power Sources 342 (2017) 489-494. https://10.1016/j.jpowsour.2016.12.079.

[30] Émond N, Torriss B, Morris D, Chaker M, Natural metamaterial behavior across the phase transition for $W_xV_{1-x}O_2$ films revealed by terahertz spectroscopy, Acta Materialia 140 (2017) 20-30. https://10.1016/j.actamat.2017.08.029.

[31] Wan J, Ren Q, Wu N, Gao Y, Density functional theory study of M-doped (M = B, C, N, Mg, Al) VO_2 nanoparticles for thermochromic energy-saving foils, Journal of Alloys and Compounds 662 (2016) 621-627. https://10.1016/j.jallcom.2015.12.100.

[32] Wan M, Xiong M, Li N, Liu B, Wang S, Ching W-Y, Zhao X, Observation of reduced phase transition temperature in N-doped thermochromic film of monoclinic VO_2, Applied Surface Science 410 (2017) 363-372. https://10.1016/j.apsusc.2017.03.138.

[33] Ren Q, Wan J, Gao Y, Theoretical Study of Electronic Properties of X-Doped (X = F, Cl, Br, I) VO_2 Nanoparticles for Thermochromic Energy-Saving Foils, The Journal of Physical Chemistry A 118 (2014) 11114-11118. https://10.1021/jp5092448.

[34] Jiang M, Li Y, Li S, Zhou H, Cao X, Bao S, Gao Y, Luo H, Jin P, Masuda Y, Room Temperature Optical Constants and Band Gap Evolution of Phase Pure M1-VO_2 Thin Films Deposited at Different Oxygen Partial

Pressures by Reactive Magnetron Sputtering, Journal of Nanomaterials 2014 (2014) https://10.1155/2014/183954.

[35] Zylbersztejn A, Mott N F, Metal-insulator transition in vanadium dioxide, Physical Review B 11 (1975) 4383-4395. https://10.1103/PhysRevB.11.4383.

[36] Zhao L, Ou W, Ma J, Zhu H, Feng M, Liu J, The enhancement of the infrared switching efficiency and laser protection performance of VO$_2$ film with Ta gradient doping, Vacuum 233 (2025) https://10.1016/j.vacuum.2024.113984.